OPEN ACCESS
IOP Publishing
Nanotechnology

Nanotechnology **36** (2025) 125302 (13pp) https://doi.org/10.1088/1361-6528/adab7c

Fabrication of hierarchical sapphire nanostructures using ultrafast laser induced morphology change

Joshua Cheung, Kun-Chieh Chien, Peter Sokalski, Li Shi and Chih-Hao Chang*

Walker Department of Mechanical Engineering, The University of Texas at Austin, Austin, TX 78712, United States of America

E-mail: chichang@utexas.edu

Received 8 November 2024, revised 7 January 2025
Accepted for publication 17 January 2025
Published 30 January 2025

Abstract

Sapphire is an attractive material that stands to benefit from surface functionalization effects stemming from micro/nanostructures. Here we investigate the use of ultrafast lasers for fabricating sapphire nanostructures by exploring the relationship between irradiation parameters, morphology change, and selective etching. In this approach a femtosecond laser pulse is focused on the substrate to change the crystalline morphology to amorphous or polycrystalline, which is characterized by examining different vibrational modes using Raman spectroscopy. The irradiated regions are removed using a subsequent hydrofluoric acid etch. Laser confocal measurements quantify the degree of selective etching. The results indicate a threshold laser pulse intensity required for selective etching. This process was used to fabricate hierarchical sapphire nanostructures over large areas with enhanced hydrophobicity, with an apparent contact angle of 140 degrees, and a high roll-off angle, characteristic of the rose petal effect. Additionally, the structures have high broadband diffuse transmittance of up to 81.8% with low loss, with applications in optical diffusers. Our findings provide new insights into the interplay between the light-matter interactions, where Raman shifts associated with different vibrational modes can predict selective etching. These results advance sapphire nanostructure fabrication, with applications in infrared optics, protective windows, and consumer electronics.

Supplementary material for this article is available online

Keywords: sapphire, morphology change, hierarchical nanostructures, surface functionalization, laser patterning

* Author to whom any correspondence should be addressed.

1. Introduction

Sapphire exhibits attractive properties including high mechanical hardness, broad optical transparency spectrum, and excellent chemical inertness [1–3]. These attributes make the material an ideal choice for photonic [4, 5], optoelectronic [6–8], and functional transparent ceramic applications [9, 10]. Many of these uses stand to benefit from surface functionalization using periodic arrays of micro or nanostructures. These structures can exhibit a variety of wetting states, including the Wenzel state, where the liquid fully wets the surface roughness and the Cassie–Baxter state [11, 12], where air pockets are trapped between the liquid and the structure. Both wetting states can be observed in hierarchical structures, known as the rose petal effect, where the liquid fully wets the microscale but not the nanoscale roughness [13]. Depending on the induced wetting state, these periodic arrays of nanostructures can exhibit superhydrophobic [14–17], self-cleaning [14, 18, 19], anti-fogging [20–22], antibacterial [23], or water harvesting properties [23–25]. Surface functionalization has been extensively demonstrated in conventional optics materials such as silica-based glass, which is well understood with established industry infrastructure. Unfortunately, the higher hardness and chemical stability of sapphire, which makes it desirable as a material, render many of the conventional micromachining processes ineffective [26].

Currently, several techniques exist for patterning nanostructures in sapphire, including using a multilayer mask with etching [27, 28], nanomachining with an atomic force microscopy (AFM) probe [29, 30], or ultrafast laser processing [31, 32]. Multilayer masks employ silicon-based layers paired with reactive ion etching processes to increase etch selectivity and fabricate high aspect ratio periodic nanostructures. However, this approach requires complex deposition and etch steps to create and is limited to a small set of geometries and aspect ratios [27, 28]. AFM nanomachining of sapphire utilizes a diamond probe to physically scribe into the surface of the substrate [29, 30]. While this process allows for high-resolution patterning, the restrictions of the tip geometry and the low throughput of the serial process severely constrain practical applications. Ultrafast lasers feature high pulse intensities in very short periods of time which results in the transient nonlinear multiphoton absorption and avalanche ionization processes, leading to material removal and the creation of long-lived defects in the substrate [31–35]. The accumulation of defects seeds subsequent excitation, resulting in an increased effective absorption coefficient that reduces the damage threshold for subsequent pulses [32, 35]. This process can be used to direct-write micro and nanostructures into sapphire substrates using ablation, or combined with wet etching processes such as laser-induced carbothermal reduction, allowing for the micromachining of arbitrary geometries and even the creation of nanostructures below the substrate surface [36–39]. However, these processes suffer from defects and poor surface quality in certain conditions due to thermal and mechanical damage. In addition, the performance of direct-write ultrafast laser nanostructure fabrication depends heavily on the combination of ablation and morphology change mechanisms taking place, which is not well understood.

Ablation using ultrafast lasers with fs pulses can induce high laser pulse intensities, on the order of 10^{13} W cm^{-2} [40], with which the substrate is directly converted from a solid to a gaseous state. The ablation mechanism benefits from being a single step process with few pre-processing or post-processing requirements [26]. However, this process is often violent, with debris, cracks, and other defects resulting from the phase change and high thermal load inherent to ablation [41, 42]. The ablation of sapphire via ultrafast laser is well understood and has been thoroughly investigated in other works [33–35, 43]. Simulations of sapphire ablation with femtosecond lasers using finite element method models based on free electron density have been shown to strongly agree with experimental results [33, 34]. Furthermore, the damage thresholds for femtosecond laser ablation of sapphire have been experimentally characterized with respect to pulse count across various pulse duration regimes and repetition rates [35, 43]. In these studies an inverse relationship between the damage threshold and pulse count have been observed, asymptotically approaching a minimum threshold at high pulse counts due to a saturation of multiphoton absorption and avalanche ionization effects [35, 43]. Ultrafast laser irradiation has also been demonstrated to change the morphology of the sapphire substrate from single crystal to polycrystalline and amorphous [44]. The increase in grain boundaries in the polycrystalline and amorphous regions corresponds to higher etch rates with respect to the bulk substrate, with selectivity ratios as high as 1:10^4 being reported for hydrofluoric acid (HF) [44–47]. This difference in etch rates according to morphology allows for the maskless selective etching of the modified regions via dry or wet etching processes, resulting in the creation of surface structures [42, 44, 48–54]. Additionally, the lower thermal loads present and surface refinement inherent to the etching process results in fewer defects compared to ablation [48]. While other works have studied sapphire morphology change using transmission electron microscopy [44], little research has been dedicated to understanding the effect of ultrafast laser parameters on the induced morphology change in sapphire. In addition, a knowledge gap exists between the morphology state of sapphire and its effect on selective etching.

In this work, we investigate the ultrafast laser induced morphology change of single-crystal sapphire using Raman spectrometry and harness this process to pattern hierarchical nanostructures. In this approach the micro-Raman measurements are employed to give insight into the crystallinity of the laser modified regions and identify the key vibrational modes that correspond to morphology change. Additionally, the irradiated sapphire regions are etched using HF, which features a combination of high etch selectivity and high etch rate [45]. This allows for a better understanding of the relationship between morphology state and the degree of selective etching. While other sapphire etchants such as sodium hydroxide (NaOH), potassium hydroxide (KOH), and a mixture of sulfuric and phosphoric acid (H_2SO_4 and H_3PO_4) are available, they exhibit lower etch rates in the case of NaOH and KOH, or

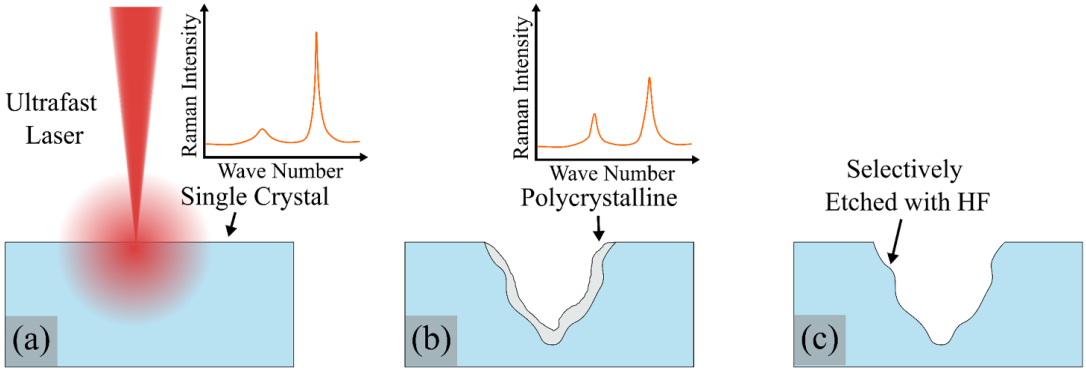

Figure 1. Proposed nanostructure fabrication process. Diagram of (a) sapphire substrate irradiated with an ultrafast laser, (b) the resulting region with ablation and morphology change to polycrystalline, and (c) the structure after HF etching.

reduced etch selectivity when using H_2SO_4 and H_3PO_4 [45]. Consequently, HF was selected as the etchant for this study to ensure efficient material removal and explore the relationship between morphology state and the degree of selective etching. Laser confocal measurements taken before and after the etch process allows the selective etching of the modified regions to be quantified with respect to laser irradiation conditions, the Raman peaks, and the morphology state. Lastly, the process is used to demonstrate the large-area surface functionalization of sapphire using ultrafast laser induced nanostructures. The resulting nanopatterned surface exhibits high contact angles (CAs) and high roll-off angles, characteristics of rose petal effect, which is useful for antibacterial and water harvesting purposes. Additionally, specular and diffuse UV–Vis–NIR transmission measurements of the nanostructures demonstrates an efficient broadband optical diffuser. This work improves the understanding of sapphire morphology change via ultrafast laser and the corresponding selective etching, which can enable new sapphire nanomanufacturing processes with applications in photonics, optoelectronics, and transparent ceramics.

2. Experimental methodology

The ultrafast morphology modification and patterning process is illustrated in figure 1. First, the single-crystal sapphire substrate (MSE Supplies, 2 inch sapphire wafer c-plane, double side polish 300 μm thick) in figure 1(a) is irradiated with ultrafast laser (Spectra-Physics Solstice Ace), resulting in the ablation and morphology change seen in figure 1(b). The irradiated region is then etched in 49% HF for 60 min at room temperature to remove the polycrystalline areas, resulting in the structure shown in figure 1(c). The experimental setup used for the direct-write experiments is described in supporting information section A.

The effects of laser intensity and pulse count on morphology change and the subsequent selective etching in sapphire substrate is explored using a matrix of direct-write spots. Laser pulse count varies across the x-axis of the test matrix while laser pulse intensity varies across the y-axis of the test matrix. An adjustable-speed electronic shutter (Vincent Associates VS25 25 mm optical shutter) provides control over the pulse count. The pulse peak intensity I_{peak} is determined by:

$$I_{\text{peak}} = \frac{P}{\tau \cdot A \cdot f} \tag{1}$$

where the average power P is measured using an optical power meter, spot area A is calculated based on the full width at half maximum (FWHM) beam diameter measured using the camera. Pulse duration τ and repetition rate f are 50 fs and 1 kHz, respectively, for the ultrafast laser used. The pulse intensity is controlled by altering the nominal power of the ultrafast laser, with all other parameters kept constant. Initially, a 5×5 reference grid is patterned onto the sapphire substrate using ablation to track the position of each irradiation spot. After creating the grid, direct-write spots are irradiated in the center of each of the spaces as illustrated in figure 1(a). The direct-write spots are patterned with laser parameters in accordance to their position in the test matrix. The laser pulse count varies linearly from 10 pulses to 50 pulses across the x-axis while the laser intensity varies exponentially from 160 TW cm^{-2} to 2560 TW cm^{-2} across the y-axis.

To understand the morphology changes induced by the ultra-fast laser and the subsequent selective etching, the crystallinity and feature profiles, as shown in figure 1(b), are measured prior to the etching processes. The morphology is characterized by measuring the Raman spectra using a custom-built system alongside a commercial system with spatial mapping (Witec, micro-Raman Spectrometer Alpha 300). The Raman measurements are performed using a green laser with an excitation wavelength of 532 nm and an approximately 2 μm beam spot diameter. Following the pre-etch measurements, the sapphire wafer is immersed in 49% HF acid for 60 min at room temperature to selectively etch the regions with amorphous or polycrystalline morphologies, resulting in the structure shown in figure 1(c). The three-dimensional feature profiles are measured using a laser confocal microscopy system (Keyence, VK-X1100) before and after the HF etch to demonstrate selective

etching. To quantify the degree of selective etching, the metric of etch area ratio A_{ratio} was chosen, defined by:

$$A_{\text{ratio}} = \frac{A_f - A_i}{A_i} \tag{2}$$

where A_i is the pre-etch surface cross-sectional area and A_f is the post-etch surface cross-sectional area of the sample spot, as measured by confocal microscopy. An example measurement is presented in supporting information section B.

2.1. Macroscale surface functionalization of sapphire substrate

An approximately 3.5 mm × 3.5 mm array of hierarchical sapphire structures, featuring nanoscale roughness atop the underlying microstructure with a 7 μm period, was fabricated to demonstrate hydrophobic effects resulting from surface functionalization. The ultrafast laser is scanned over a 2D dense grid with overlapping lines spaced 7 μm apart at a laser intensity of 1,155 TW cm^{-2} and an average pulse count of 9.33 along the centerline. Following the ultrafast laser modification of the sapphire surface, the sample is etched in 49% HF acid for 60 min. The post-etch samples are then cleaned using RCA clean 1 (1:1:5 mixture of 29 wt% NH_3, 30 wt% H_2O_2, and H_2O) and oxygen plasma etching (18 W for 10 min) to remove organic contaminants from the sample surface in preparation for silane coating. The cleaned sample was placed inside a vacuum chamber along with a petri dish containing several drops of trichloro(octyl)silane (97%, Sigma Aldrich) for 8 h, resulting in silane coated sapphire nanostructures. Following the application of a silane coating to reduce surface energy of the sapphire surfaces, CA measurements of the nanostructured and planar sapphire substrates were made using a goniometer (First Ten Angstroms, FTA 200). Optical properties were characterized with optical transmission measurements using a UV–Vis–NIR Spectrometer (Agilent, Cary 5000) with an external diffuse reflectance accessory using an integrating sphere (Agilent, DRA-1800). Diagrams of the patterning process and the resultant hierarchical structures can be found in supporting information section C.

3. Results and discussion

The matrix of irradiated ultrafast laser spots with various pulse intensity and count before and after HF etch are shown in the top-view SEM images shown in figure 2. Holes resulting from ablation can be observed in regions with a pulse intensity of 640 TW cm^{-2} or higher as shown in figure 2(a). Furthermore, increasing irradiation intensity and pulse count both correspond to larger holes. Following HF etching, smoothing of the planar surface and some widening of the holes can be observed in figure 2(b). Additionally, cracks can be identified in the corners of the post-etch grid. Changes in the feature profiles and etched areas will be discussed in a later section.

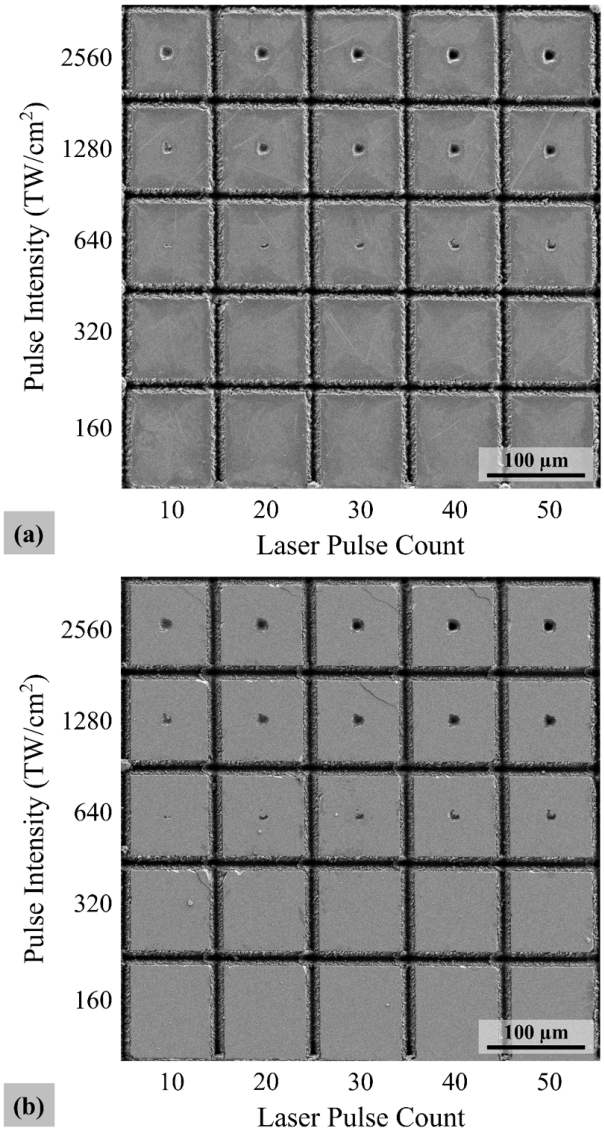

Figure 2. Matrix of samples before and after wet etching via HF acid. (a) SEM image of the sample matrix before etching, with laser pulse count and laser intensity varying along the x and y axes, respectively. (b) Corresponding SEM image of the sample matrix after etching in HF for 60 min.

Morphology change of the crystalline sapphire to amorphous and polycrystalline states via ultrafast laser is a key mechanism to selective etching. The measured Raman spectra for the irradiated and pristine sapphire are shown in figure 3. For the sapphire substrate, the measured spectrum shows characteristic peaks at 382, 420, 433, 452, and 580 cm^{-1}. Notably, the 420 cm^{-1} peak corresponds to the A_{1g} vibrational mode while the remaining peaks exhibit an E_g vibrational mode [55, 56]. It can be observed that the pristine sapphire has a higher 420 cm^{-1} peak and a lower 382 cm^{-1} peak compared with the

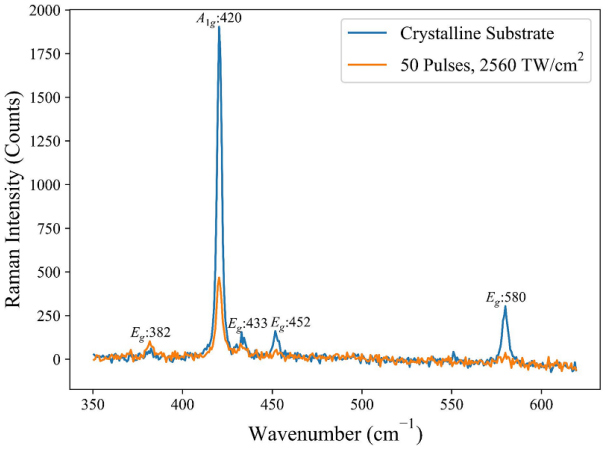

Figure 3. Comparison of Raman spectra between the crystalline substrate and an amorphous region. The Raman spectra of the crystalline substrate and region irradiated with 50 pulses at 2560 TW cm^{-2}. Several distinct peaks for the c-plane sapphire substrate can be observed, with the most prominent being the 420 cm^{-1} peak.

irradiated regions. It is important to note that due to variations in topography and the resulting differences in the scattering of the excitation light, direct comparisons of Raman intensities cannot be made accurately. Instead, the ratio of E_g to A_{1g} vibrational modes corresponding to 382 cm^{-1} and 420 cm^{-1} peaks will serve as the metric for comparing the degree of crystallinity for the irradiated regions to mitigate the effects of the aforementioned scattering. Other methods for analyzing the Raman spectra were explored, including using the FWHM of the 420 cm^{-1} peak as described in supporting information section D, however the results were difficult to interpret due to measurement noise and system limitations. The 382 cm^{-1} and 420 cm^{-1} Raman peaks for the crystalline substrate have intensity counts of 61 and 1901 respectively, resulting in an E_g to A_{1g} ratio of 0.03. In contrast, for the most intense irradiated region with 2560 TW cm^{-2} and 50 pulses, the 382 cm^{-1} and 420 cm^{-1} peaks have intensity counts of 101 and 465 respectively, resulting in a ratio of 0.22. This difference can be attributed to the selective excitation of different vibrational modes corresponding to different laser polarization directions with respect to the crystal [56]. As such, the Raman peaks are sensitive to the crystal orientation of the sapphire substrate. Since the Raman measurement parameters are held constant, deviations in the peaks corresponding to E_g and A_{1g} modes indicates that the crystal orientation has been altered by the ultrafast laser irradiation and is no longer purely c-plane sapphire, but rather a combination of different orientations, pointing to the polycrystalline nature of the irradiated spot. As such, lower E_g to A_{1g} ratios correspond to higher degrees of crystallinity, which is observed in the pristine sapphire. Understanding the relationship between the vibrational modes and morphology change helps to understand the parameters of laser pulse count and laser intensity, which are system specific, into morphology states which may be broadly applied.

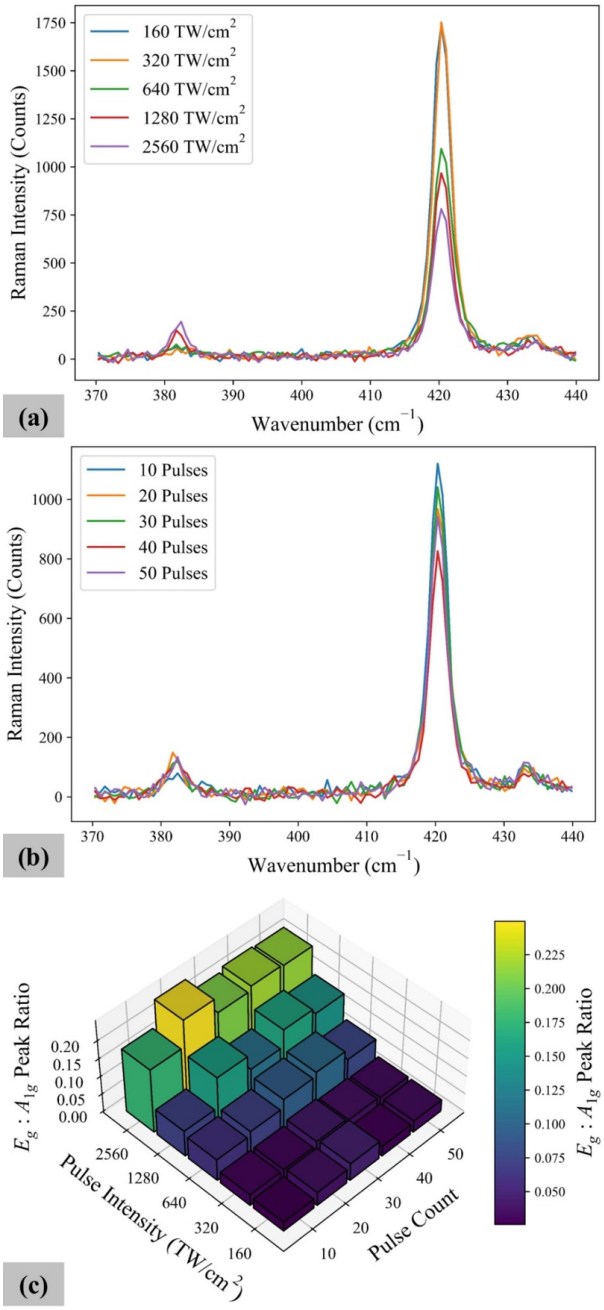

Figure 4. Micro-Raman measurements of the testing matrix. (a) Measured Raman spectra for spots with 160 TW cm^{-2} to 2560 TW cm^{-2} peak intensity and constant 20 pulses. (b) Raman spectra or spots with 10–50 pulses at constant peak intensity of 1280 TW cm^{-2}. (c) Plot of the E_g to A_{1g} ratio for each irradiated region at the center of the spot.

The measured Raman spectra for regions irradiated with varying intensity and pulse count are shown in figures 4(a) and (b), respectively. The pulse count is held constant at 20 for figure 4(a), where irradiation at low pulse intensities has little influence on the characteristic E_g to A_{1g} ratio

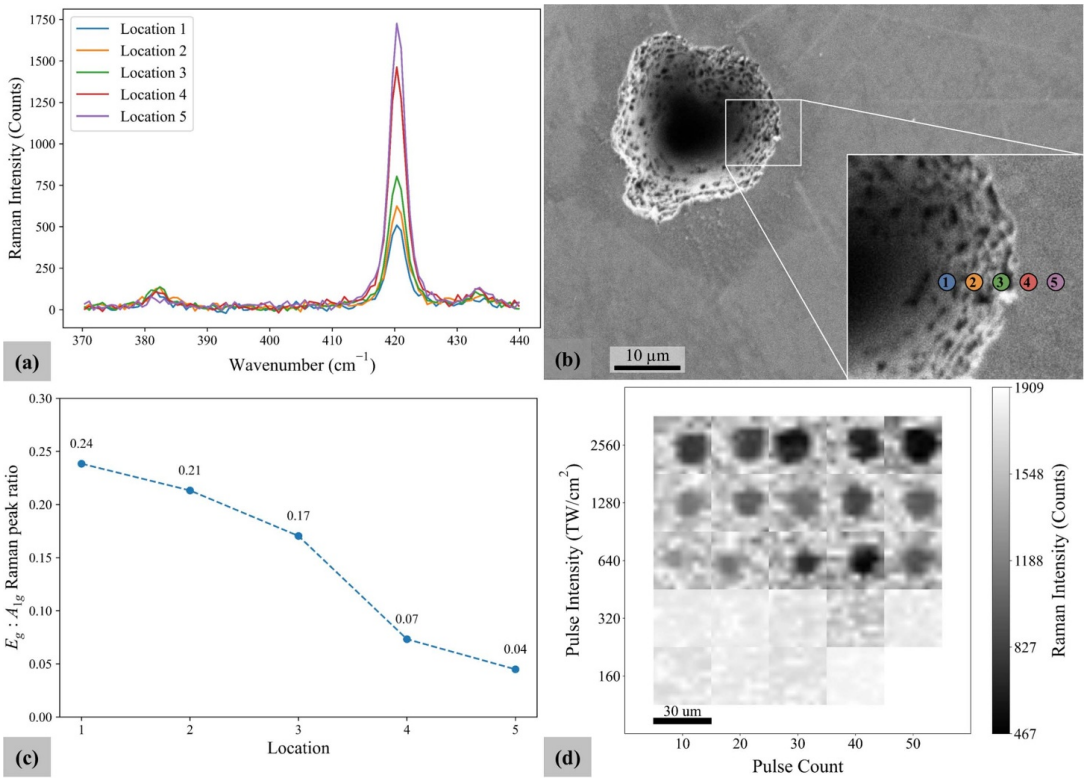

Figure 5. Micro-Raman measurements from along the transition from amorphous and polycrystalline to crystalline. (a) Micro-Raman spectra for each of the five locations across the boundary for the 1280 TW cm^{-2} pulse intensity and 50 pulse spot. (b) Pre-etch SEM image of the irradiated spot depicting the corresponding locations denoted in part a. (c) Plot of the E_g to A_{1g} ratio at each location. (d) Plot of the micro-Raman spatial mapping of the 420 cm^{-1} peak for each of the spots. Each map is 30 μm wide, centered on the irradiated spot, the rest of the grid is not pictured.

as noted by the similar 382 cm^{-1} and 420 cm^{-1} peaks. A threshold intensity of around 640 TW cm^{-2} can be noted before significant change in the peaks can be observed. Past the threshold, increases in pulse intensity further increases the 382 cm^{-1} peak and decreases the 420 cm^{-1} peak. The Raman spectra for spots with constant intensity of 1280 TW cm^{-2} and variations in pulse counts are displayed in figure 4(b), from which the pulse counts appear to have little effect on either 382 cm^{-1} or 420 cm^{-1} peaks. The relatively high pulse counts present may have resulted in the saturation of morphology change effects, preventing any pulse count trends from being observed. The measured E_g to A_{1g} ratios for the entire experimental matrix are plotted in figure 4(c) to illustrate the degree of crystallinity of each irradiated spot. Based on the bar graph, the aforementioned threshold is observed across all pulse counts, reinforcing the existence of a threshold irradiation intensity required for morphology change.

In addition to the changes in morphology due to laser irradiation parameters, the spatial variation of the pattern spot is also examined, as shown in figure 5. Here the spot irradiated with 50 pulses at 1280 TW cm^{-2} is used as a representative case. The changes in the measured Raman spectra moving from location 1, with higher laser irradiation, to location 5, which features a morphology similar to that of the crystalline substrate can be seen in figure 5(a). The decrease in the A_{1g} mode can be observed in the 420 cm^{-1} peak, while changes to the E_g mode located at 382 cm^{-1} are less discernible. The corresponding locations across the spot boundary are depicted in the SEM image shown in figure 5(b), which demonstrates the short length scales of approximately 5 μm in which the transition from amorphous and polycrystalline to fully crystalline occurs. The E_g to A_{1g} ratio of the five locations are plotted in figure 5(c), with a trend of increasing crystallinity moving from location 1 to location 5.

The spatial variation of morphology for the matrix of spots is investigated in figure 5(d), using micro-Raman mapping of the 420 cm^{-1} peak intensities. Despite not being as robust of a metric as E_g to A_{1g} ratios, 420 cm^{-1} peak intensities are used in the micro-Raman mapping due to the sensitivity limitations of the micro-Raman Spectrometer Alpha 300 in measuring the smaller 382 cm^{-1} peaks. The map of each spot has been linearly interpolated with respect to crystalline sapphire and the most amorphous measurement, allowing for comparison between the spots. The lack of discernible spots at lower intensities supports the notion of

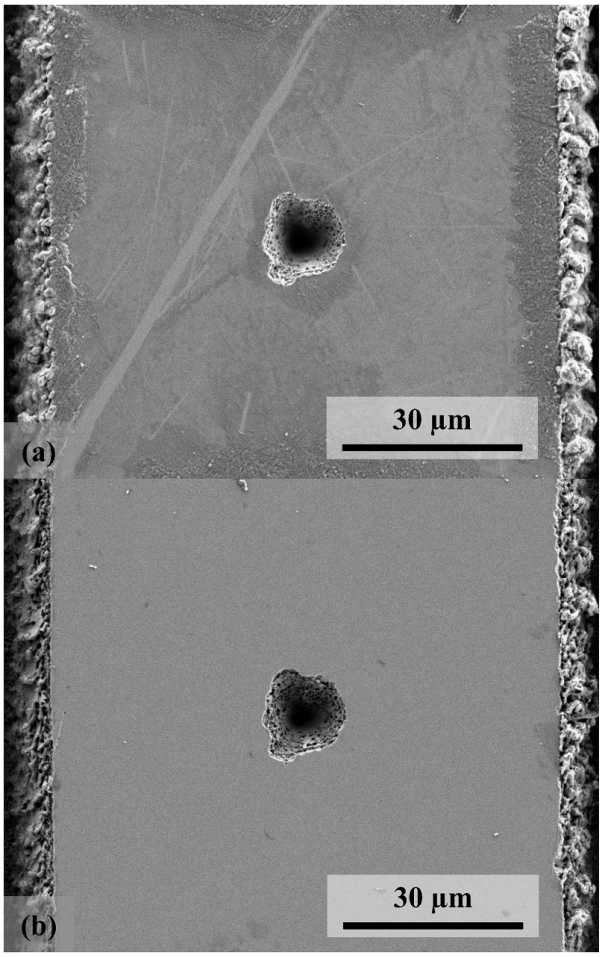

Figure 6. Top-view SEM of 1280 TW cm^{-2} and 50 pulses irradiated region before and after etch. (a) SEM image of the spot irradiated with 1280 TW cm^{-2} and 50 pulses before etching. Note the marks and rough surface present. (b) SEM image of the spot post etch.

a threshold irradiation intensity for morphology change to occur. Irradiated regions above the intensity threshold feature a mostly uniform amorphous or polycrystalline spot with a short transition to the crystalline background. This reinforces the short transition length scales found in figure 5(b).

With the effects of laser parameters and spatial variation on morphology better understood, the impacts on selective etching are investigated next. Figures 6(a) and (b) below shows the 1280 TW cm^{-2} and 50 pulses region before and after the HF etch. The etch selectivity of concentrated HF for crystalline vs polycrystalline/amorphous is as high as 1:10^4, ensuring only the material with modified morphology will be removed [44, 45]. Note the improved surface finish and the removal of material at the edges of the reference grid as a result of the etch. The edges of the spot are similarly etched, and pores can be observed inside the spot by the selective removal of amorphous and polycrystalline material. Analysis of figures 2(a) and (b) reveals a similar trend across the entire matrix of spots, with effects of the HF etch observed in the widening of the reference grid lines and the smoothing of the plane surface.

To better understand selective etching due to morphology change, the profile of the pattern can be extracted from the confocal microscope data, as shown in figure 7. Here figures 7(a)–(c) depict the pre-etch and post-etch cross-sectional profiles for the 640, 1280, and 2560 TW cm^{-2} spots at 20 pulses, respectively. The post-etch profiles feature a slight broadening of the width when compared to the pre-etch profiles, with the width increasing by approximately 0.8, 1.1, and 1.4 μm for the 640, 1280, and 2560 TW cm^{-2} spots, respectively. A similar increase in depth is observed, where the post-etch profile is deeper by approximately 0.4, 0.7, and 0.8 μm for the corresponding samples. The contours appear to maintain similar topographic profiles before and after the HF etch, likely a result of the isotropic nature of wet etch processes as well as the relatively small etch depths present. Note the high surface roughness present on the surface of the pre-etch profiles, a result of the defects and ejecta resulting from laser irradiation. In contrast, the smoother surface profiles for the post-etch spots are caused by the removal of the polycrystalline and amorphous material in the wet-etch process.

The etch area ratio, as defined by equation (2), for each spot in the testing matrix is shown in figure 7(d). Note the lack of etch area ratio for irradiated regions with laser intensities of 160 TW cm^{-2} and 320 TW cm^{-2}, indicating a minimum pulse intensity threshold before any selective etching can occur. Other metrics were explored, such as the change in maximum depth of the spots before and after etching. However, difficulties were encountered in resolving the bottom of the high pulse count and intensity spots using laser confocal microscopy as demonstrated in supporting information section E. Across the irradiated regions, the maximum measured depth was 14.1 μm, at which point the reflection signal was too low. Paired with the high noise levels inherent to point-based measurements, these two measurement limitations guided the choice of etch area ratio as the preferred metric for selective etching.

The relationship between laser irradiation parameters and etch area ratio are reinforced in figure 8. Here the etched area ratios are plotted versus pulse intensity and pulse count in figures 8(a) and (b), respectively. The previously observed threshold intensity is supported in figure 8(a), where selective etching does not occur at pulse intensities below 640 TW cm^{-2}. In pulse intensity regimes where selective etching takes place, there is no significant correlation between pulse intensity and etch area ratio, with no recognizable patterns in the constant pulse count lines past the threshold, as shown in figure 8(a). Furthermore, pulse count does not have a significant influence on etch area ratio, as indicated by the lack of clear trends in the constant pulse intensity lines in figure 8(b). One explanation for this result can be the relatively high pulse count floor of 10 tested, where the morphology change effect has already saturated. The pulse number is expected to have an effect on the selective etch and morphology change at lower pulse counts below 10, which is the subject of on-going efforts. The etch area ratio is plotted versus

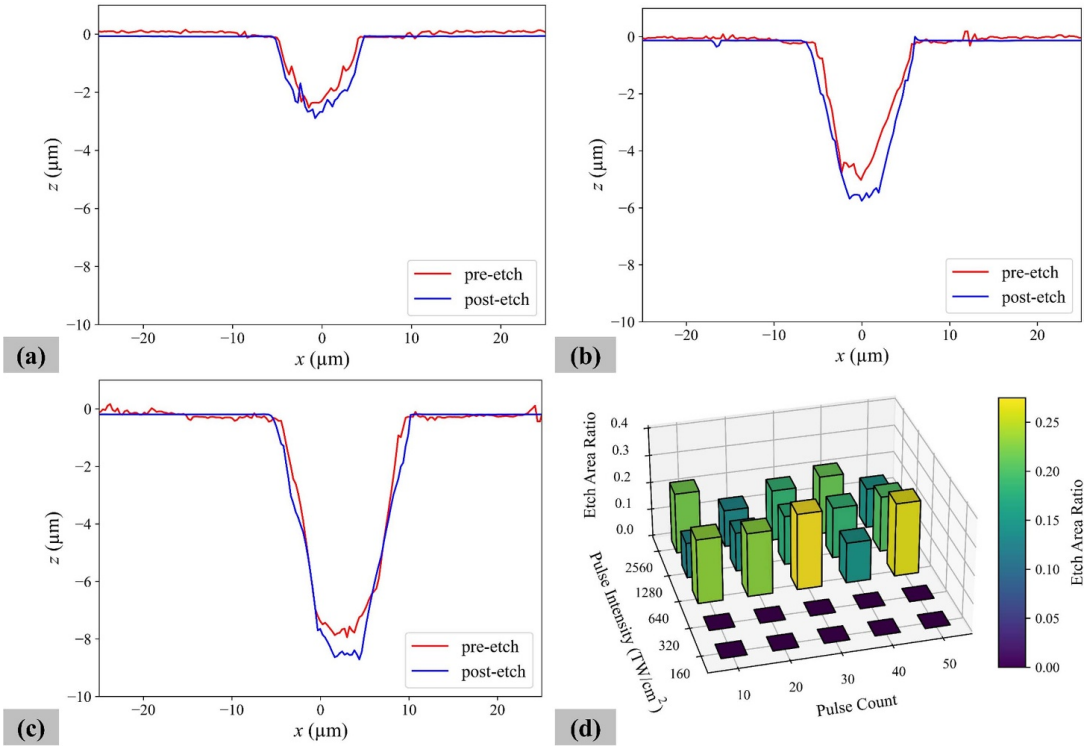

Figure 7. Selective etch results using confocal microscopy. Measured pre-etch and post-etch profiles for the 20 pulses spots with irradiation intensity of (a) 640, (b) 1280, and (c) 2560 TW cm^{-2}. (d) Bar graph detailing the etch area ratio for each of the 25 combinations of pulse intensity and pulse count parameters.

the measured E_g to A_{1g} ratio in figure 8(c) and corroborates the existence of a morphology state threshold necessary for selective etching to occur. Moreover, a further increase in Raman E_g to A_{1g} ratios beyond the threshold appears to have less effect on etch area ratio. As such, figure 8(c) describes a binary relationship between selective etching and the morphology state, with two distinct etching and non-etching phases. This result also indicates that the crystallinity measured by Raman spectra can be an accurate predictor of the final features after wet etching. Additional examples of the observed trends can be seen in the SEM images, confocal height maps, and Raman spectra of the 20 pulse spots found in supporting information section F.

3.1. Hydrophobic surface functionalization demonstration

To demonstrate surface functionalization using ultrafast laser induced morphology change and the subsequent selective etching, sapphire nanostructures are patterned over an area of 12.25 mm^2, as seen in figure 9(a). Static CA measurements and roll-off angle measurements of the sapphire nanostructures are shown in figure 9(b). The SEM image of the post-etch sapphire structures shown in figure 9(c) reveals the micrometer-scale periodicity of the structures, while figure 9(d) exhibits the nanometer-scale roughness atop the underlying microstructures. Together, these features on two different length scales as shown in figures 9(c) and (d) constitute a hierarchical structure. The period and height of the microstructure are measured to be 7 and 5.7 μm, respectively. The surface was measured with confocal microscopy to have a roughness factor of 2.34. However, the measurements are limited by the system resolution and do not account for all the nanometer-scale features, as seen in the heightmap found in supporting information section G. This surface roughness is a critical component of hydrophobicity in accordance with the Wenzel equation [15]

$$\cos\theta^* = r\cos\theta \tag{3}$$

where θ is the CA with a flat surface, r is the roughness factor, and θ^* is the apparent CA. Prior to silanization, the flat sapphire substrate and sapphire nanostructures exhibited hydrophilic CAs of 57 degrees and 52 degrees, respectively. With the silane coating, the CA for the flat sapphire substrate was measured in figure S12(a) to be 106 degrees, which is hydrophobic. The CA of the silane coated sapphire nanostructures was measured at 140 degrees in figure S12(b), exhibiting a marked improvement of 34 degrees over the sapphire substrate due to the hierarchical structure. Moreover, the nanostructures have a higher CA than the 130 degrees predicted by the Wenzel model. Such improvements in CA, nearing the superhydrophobic regime of 150 degrees, can be attributed

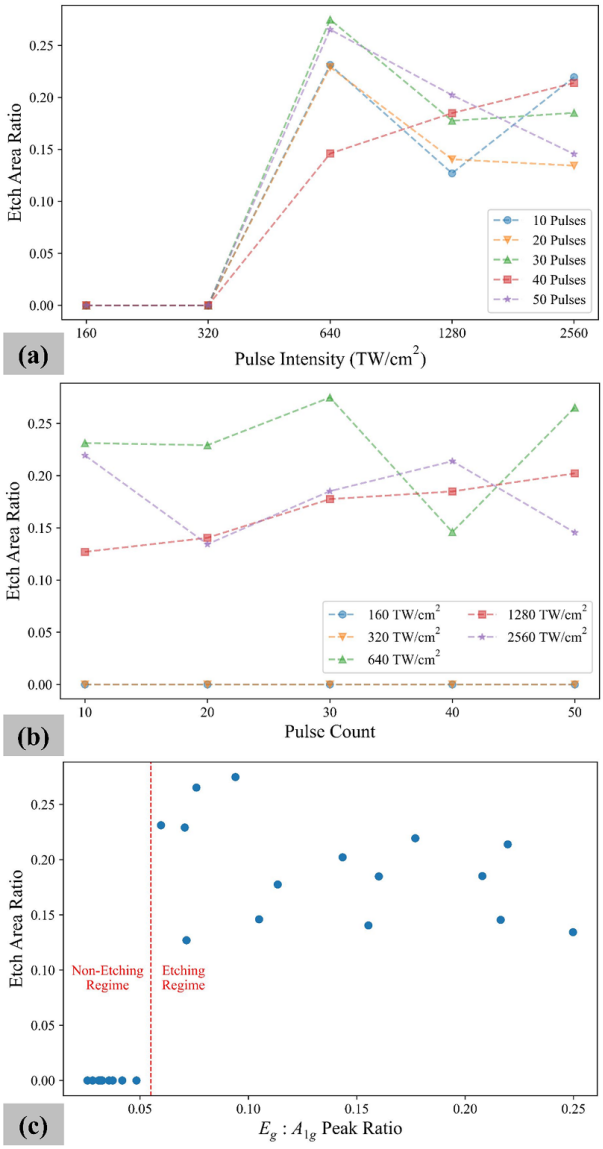

Figure 8. Correlations between laser parameters and Raman spectra to selective etching. (a) Graph of etch area ratio as a function of (a) pulse intensity and (b) pulse count. (c) Graph of etch area ratio as a function of Raman E_g to A_{1g} ratio measured using Raman microscopy.

to the hierarchical nature of the sapphire structures. Roll-off angle measurements of the hierarchical sapphire nanostructures in figure 9(b) indicate that the drop does not roll off even when perpendicular, indicating high CA hysteresis (CAH). The high liquid adhesion paired with the high static CA is characteristic of the rose petal effect, which can be attributed to the liquid wetting the microstructure but not the nanoscale roughness [19, 23, 24]. The unique combination of high CA and high CAH has applications in antibacterial, water harvesting, and guided fluid transport surfaces [19, 23–25]. Detailed goniometer measurements are described further in supporting information section H.

The optical transmission characteristics of sapphire are also critical for many applications and are characterized for the fabricate sample. The specular and diffuse transmittance measurements for the planar and nanostructured sapphire substrates are illustrated in figure 10. The specular and diffuse transmittance of the sapphire substrate have an average of 83.2% and 4.1%, respectively, across the range of wavelengths from 250 nm to 2500 nm. The high specular and low diffuse transmittance for the sapphire substrate is characteristic of optical windows, as expected from the polished surfaces. Conversely, the nanostructures demonstrate the opposite behavior, with an average specular and diffuse transmission of 11.9% and 73.9%, respectively. A peak diffuse transmittance of 81.8% can be observed at 1354 nm wavelength and maintains this value until gradually falling at longer wavelengths. The micro/nanoscale roughness of the hierarchical structures induces light scattering that results in predominantly diffuse transmission. Note that the total transmission of the planar and nanostructured samples across the measured wavelength are nearly identical as described in supporting information section I, with averages of 87.4% and 85.8%, respectively. The total transmission of the nanostructured sapphire sample is even higher than the substrate at wavelengths longer than 1600 nm, reaching a peak of 96.1% at 2135 nm. Consequently, the nanostructures exhibit 98.2% of the substrate total transmission, demonstrating low optical losses. Furthermore, the flat trends of the nanostructure transmittance measurements across the visible to infrared point to the broadband nature of their optical behavior. The efficient broadband diffuse characteristics of the sapphire nanostructures make them suitable for applications in laser illumination [57], optical sensors [58], and display technologies [59]. Furthermore, the combination of rose petal effects and diffuse optical properties exhibited by the sapphire nanostructures constitutes a high-performance antifouling optical diffuser [60] suitable for chemical sensors [61, 62], daylight harvesting [63, 64], and medical applications [65, 66]. Notably, the hierarchical sapphire nanostructures perform similarly to other nanoscale approaches to self-cleaning optical diffusers. For example, PDMS Morpho-type diffusers created using nanoimprint lithography exhibit a static CA of 134 degrees and a mean diffuse transmission of 78.8% [60], compared to the 140 degrees and 73.9% observed for the ultrafast laser fabricated sapphire nanostructures in this work.

4. Discussion and future work

The laser irradiation results demonstrated clear relationships between irradiation parameters and the subsequent selective etching in HF, namely the presence of a threshold pulse intensity around 640 TW cm^{-2} necessary for etching to occur. The data also indicates the lack of any strong trends between pulse count and selective etching, which can be attributed to the relatively high pulse numbers tested. The

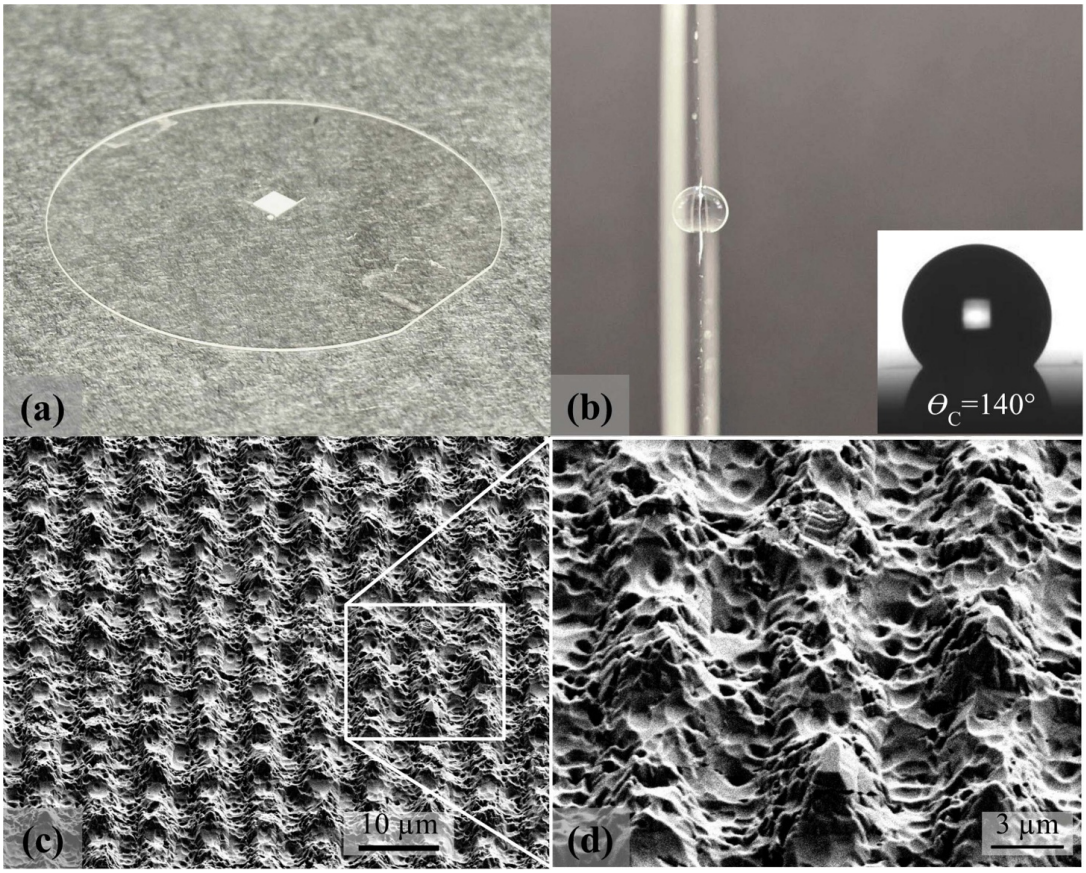

Figure 9. Demonstration of hydrophobic effects induced by sapphire nanostructures created via ultrafast laser. (a) Image of the 3.5 mm by 3.5 mm patch of sapphire nanostructures created using ultrafast laser irradiation (center of 100 mm wafer). Subsequent HF etching and silane coating were performed to induce selective etching and increase water CA respectively. (b) Demonstration of high CAH of the post-etch sapphire nanostructures coated in silane. An inset image shows the CA measurement for the sample. (c) Angled-view SEM image of post-etch nanostructures with hierarchical features. (d) Zoomed in angled-view SEM image of post-etch nanostructures demonstrating nanoscale roughness atop the underlying periodic microscale structures.

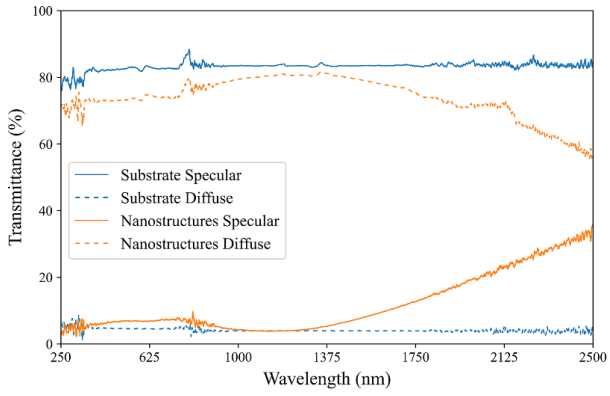

Figure 10. Optical transmittance properties of sapphire nanostructures created via ultrafast laser. Graph of diffuse and specular measurements of the post-etch sapphire nanostructures and sapphire substrate.

degree of morphology change can also be precisely characterized by using Raman microscopy, where the ratios of the intensity peaks of the E_g to A_{1g} vibrational modes correlates highly to selective etching. It is important to note the increments in pulse intensities used in this study are too coarse to accurately identify the exact threshold value, and more experiments between 320 TW cm^{-2} and 640 TW cm^{-2} are needed. Likewise, further experiments at lower pulse count regimes, namely between 1–10 pulses, are needed to avoid saturation and effectively investigate light-matter interactions within a single pulse. Additional material characterization using transmission electron microscopy and electron beam diffraction can provide morphology measurements with greater spatial resolution. By continuing to explore the relationship between morphology state, irradiation parameters, and selective etching, ultrafast laser induced selective etching can be better understood to improve the fabrication processes.

Additionally, while the macroscale sapphire nanostructure sample successfully demonstrated increased hydrophobicity by adding hierarchical roughness, further experiments are required to better understand and control the surface geometry. One key question is whether the microscale structure and nanoscale roughness can be independently controlled, which will be examined by varying the beam overlap during irradiation. Furthermore, the same roughness responsible for the nanostructures' hydrophobic effects also results in high diffuse and low specular transmission, characteristics that are undesirable for windows but are useful for optical diffusers. This roughness is a product of the violent nature of the ultrafast laser, an issue compounded by the selectivity of HF, reported to be as high as $1{:}10^4$ between crystalline and amorphous sapphire [45]. This high selectivity leaves crystalline regions virtually unetched, resulting in sharp edges and pits where local morphology varies. To address this problem, alternative etch processes will be explored to reduce the nanoscale roughness. Specifically, a mixture of H_2SO_4 and H_3PO_4 at elevated temperatures ranging from 180 °C to 270 °C will provide a lower etch selectivity of approximately 1:66 and a higher etch rate [45, 53]. By further exploring the mechanisms of hydrophobicity present in our sample and experimenting with etching processes, it is possible to improve the optical clarity of the fabricated sapphire nanostructures while maintaining their surface functionalization.

5. Conclusion

In this work, we investigate the relationships between ultrafast irradiation parameters and selective etching and demonstrate ultrafast laser fabrication of sapphire nanostructures with enhanced hydrophobicity and light scattering properties. Using Raman microscopy, the ratio of the E_g to A_{1g} vibrational modes can identify a threshold pulse intensity necessary for selective etching to take place. Additionally, a binary relationship between the morphology state of the irradiated regions and the degree of selective etching can be observed. The results indicate that the Raman spectra can be used to quantify the degradation in crystallinity and serve as a predictive metric for selective etching. We also successfully demonstrated the fabrication of sapphire nanostructures over macroscale areas via ultrafast laser and selective etching. The surface functionalization of the sample exhibited a high apparent CA of 140 degrees and high CAH, a demonstration of the rose petal effect. Furthermore, the hierarchical surface roughness accompanying the nanostructures resulted in efficient diffuse transmission of up to 81.8% and can have applications in broadband optical diffusers. Future works will focus on investigating irradiation parameters and morphology states near the threshold to better refine our understanding of selective etching using ultrafast lasers. Additionally, we will explore secondary etching processes to control the optical properties and hydrophobic effects of the nanostructures.

Data availability statement

All data that support the findings of this study are included within the article (and any supplementary files).

Acknowledgment

This work was performed at UT Austin Texas Materials Institute (TMI), the Nanomanufacturing System for mobile Computing and Energy Technologies (NASCENT), and Texas Nanofabrication Facilities, which is supported by the National Science Foundation (NSF) as part of the National Nanotechnology Coordinated Infrastructure (NNCI) Grant NNCI-2025227. This work is funded by the Army Research Office (ARO) Grant W911NF-22-1-0124 and the National Science Foundation (NSF) Grant CBET-2343526.

ORCID iDs

Joshua Cheung https://orcid.org/0009-0003-9765-371X
Kun-Chieh Chien https://orcid.org/0000-0002-6351-4784
Peter Sokalski https://orcid.org/0000-0003-4277-4322
Li Shi https://orcid.org/0000-0002-5401-6839
Chih-Hao Chang https://orcid.org/0000-0003-4268-4108

References

[1] Qiu T, Jiang F, Wang N, Lin J, Tian Z, Wu Y, Wen Q and Lu J 2024 Atomistic understanding of the variable nano-hardness of C-plane sapphire considering the crystal anisotropy *J. Mater. Res. Technol.* **29** 4514–25
[2] Pishchik V, Lytvynov L A and Dobrovinskaya E R 2009 *Sapphire: Material, Manufacturing, Applications* (Springer)
[3] Dobrovinskaya E R, Lytvynov L A and Pishchik V 2009 *Properties of Sapphire, Sapphire* (Springer) pp 55–176
[4] Wang Y, Dong X and Hu J 2022 Feasibility analysis of sapphire compound refractive lenses for advanced x-ray light sources *Front. Phys.* **10** 908380
[5] Kefer S, Roth G-L, Zettl J, Schmauss B and Hellmann R 2022 Sapphire photonic crystal waveguides with integrated bragg grating structure *Photonics* **9** 234
[6] Chen H, Buric M, Ohodnicki P R, Nakano J, Liu B and Chorpening B T 2018 Review and perspective: sapphire optical fiber cladding development for harsh environment sensing *Appl. Phys. Rev.* **5** 011102
[7] Liu H, Sun S, Zheng L, Wang G, Tian W, Zhang D, Han H, Zhu J and Wei Z 2021 Review of laser-diode pumped Ti:sapphire laser *Microw. Opt. Technol. Lett.* **63** 2135–44
[8] Li G, Wang W, Yang W, Lin Y, Wang H, Lin Z and Zhou S 2016 GaN-based light-emitting diodes on various substrates: a critical review *Rep. Prog. Phys.* **79** 056501
[9] Zhao M, Huang Y and Kang J U 2012 Sapphire ball lens-based fiber probe for common-path optical coherence tomography and its applications in corneal and retinal imaging *Opt. Lett.* **37** 4835
[10] Yan D, Yu Z, Zou T, Lin Y, Kong W and Yang J 2022 Long-time persisting superhydrophilicity on sapphire surface via femtosecond laser processing with the varnish of TiO_2 *Nanomaterials* **12** 3403
[11] Lafuma A and Quéré D 2003 Superhydrophobic states *Nat. Mater.* **2** 457–60

[12] Bhushan B and Jung Y C 2011 Natural and biomimetic artificial surfaces for superhydrophobicity, self-cleaning, low adhesion, and drag reduction *Prog. Mater. Sci.* **56** 1–108

[13] Feng L, Zhang Y, Xi J, Zhu Y, Wang N, Xia F and Jiang L 2008 Petal effect: a superhydrophobic state with high adhesive force *Langmuir* **24** 4114–9

[14] Park K-C, Choi H J, Chang C-H, Cohen R E, McKinley G H and Barbastathis G 2012 Nanotextured silica surfaces with robust superhydrophobicity and omnidirectional broadband supertransmissivity *ACS Nano* **6** 3789–99

[15] Parvate S, Dixit P and Chattopadhyay S 2020 Superhydrophobic surfaces: insights from theory and experiment *J. Phys. Chem.* B **124** 1323–60

[16] Lee E and Lee K-H 2018 Facile fabrication of superhydrophobic surfaces with hierarchical structures *Sci. Rep.* **8** 4101

[17] Parker A R and Lawrence C R 2001 Water capture by a desert beetle *Nature* **414** 33–34

[18] Behera A, Rajak D K and Jeyasubramanian K 2022 Fabrication of nanostructures with excellent self-cleaning properties *Design, Fabrication, and Characterization of Multifunctional Nanomaterials* (Elsevier) pp 449–78

[19] Chakraborty M, Weibel J A, Schaber J A and Garimella S V 2019 The wetting state of water on a rose petal *Adv. Mater. Interfaces* **6** 1900652

[20] Son T, Yang E, Yu E, Oh K H, Moon M-W and Kim H-Y 2017 Effects of surface nanostructures on self-cleaning and anti-fogging characteristics of transparent glass *J. Mech. Sci. Technol.* **31** 5407–14

[21] Cui H, Teng C, Xie X and Qi X 2024 Durable anti-fog micro-nano structures fabricated by laser ablation of aluminum film on resin/glass *Discov. Nano* **19** 58

[22] Cebeci F Ç, Wu Z, Zhai L, Cohen R E and Rubner M F 2006 Nanoporosity-driven superhydrophilicity: a means to create multifunctional antifogging coatings *Langmuir* **22** 2856–62

[23] Parra-Vicente S, Ibáñez-Ibáñez P F, Cabrerizo-Vílchez M, Sánchez-Almazo I, Rodríguez-Valverde M Á and Ruiz-Cabello F J M 2024 Understanding the petal effect: wetting properties and surface structure of natural rose petals and rose petal-derived surfaces *Colloids Surf.* B **236** 113832

[24] Szczepanski C R, Guittard F and Darmanin T 2017 Recent advances in the study and design of parahydrophobic surfaces: from natural examples to synthetic approaches *Adv. Colloid Interface Sci.* **241** 37–61

[25] Wang C, Shao R, Wang G and Sun S 2021 Hierarchical hydrophobic surfaces with controlled dual transition between rose petal effect and lotus effect via structure tailoring or chemical modification *Colloids Surf.* A **622** 126661

[26] Cuero B, Chien K-C and Chang C-H 2023 *In situ* metrology of direct-write laser ablation using optical emission spectroscopy *J. Vac. Sci. Technol.* B **41** 062603

[27] Chen Y-A, Chien K-C, Chen I-T and Chang C-H 2022 Sapphire nanophotonics: fabrication challenges and optical properties *Micro Nano Eng.* **14** 100115

[28] Chen Y-A, Chen I-T and Chang C-H 2019 Increasing etching depth of sapphire nanostructures using multilayer etching mask *J. Vac. Sci. Technol.* B **37** 061606

[29] Lin Z-C and Hsu Y-C 2012 A calculating method for the fewest cutting passes on sapphire substrate at a certain depth using specific down force energy with an AFM probe *J. Mater. Process. Technol.* **212** 2321–31

[30] Huang J-C and Weng Y-J 2014 The study on the nanomachining property and cutting model of single-crystal sapphire by atomic force microscopy: nanomachining and cutting model of sapphire *Scanning* **36** 599–607

[31] Du C, Wang Q, Zhao S and Deng X 2023 Biological sensors based on long period fiber grating *Opt. Laser Technol.* **158** 108936

[32] Balling P and Schou J 2013 Femtosecond-laser ablation dynamics of dielectrics: basics and applications for thin films *Rep. Prog. Phys.* **76** 036502

[33] Cai X, Ji C, Li C, Tian Z, Wang X, Lei C and Liu S 2021 Multiphoton absorption simulation of sapphire substrate under the action of femtosecond laser for larger density of pattern-related process windows *Micromachines* **12** 1571

[34] Wang M, Mei W and Wang Y 2019 Simulation of femtosecond laser ablation sapphire based on free electron density *Opt. Laser Technol.* **113** 123–8

[35] Wang X C, Lim G C, Zheng H Y, Ng F L, Liu W and Chua S J 2004 Femtosecond pulse laser ablation of sapphire in ambient air *Appl. Surf. Sci.* **228** 221–6

[36] Shaheen M E, Gagnon J E and Fryer B J 2015 Experimental study on 785 nm femtosecond laser ablation of sapphire in air *Laser Phys. Lett.* **12** 066103

[37] Eberle G, Schmidt M, Pude F and Wegener K 2016 Laser surface and subsurface modification of sapphire using femtosecond pulses *Appl. Surf. Sci.* **378** 504–12

[38] Liu H, Li Y, Lin W and Hong M 2020 High-aspect-ratio crack-free microstructures fabrication on sapphire by femtosecond laser ablation *Opt. Laser Technol.* **132** 106472

[39] Yan T, Ji L and Hong M 2022 Backside wet etching of sapphire substrate by laser-induced carbothermal reduction *Opt. Laser Technol.* **149** 107900

[40] Christensen M N, Byskov-Nielsen J, Christensen B H and Balling P 2010 Single-shot ablation of sapphire by ultrashort laser pulses *Appl. Phys.* A **101** 279–82

[41] Gedvilas M and Račiukaitis G 2020 Spatial zigzag evolution of cracks in moving sapphire initiated by bursts of picosecond laser pulses for ultrafast wafer dicing *RSC Adv.* **10** 33213–20

[42] Capuano L, Tiggelaar R M, Berenschot J W, Gardeniers J G E and Römer G R B E 2020 Fabrication of millimeter-long structures in sapphire using femtosecond infrared laser pulses and selective etching *Opt. Lasers Eng.* **133** 106114

[43] Uteza O, Bussière B, Canova F, Chambaret J-P, Delaporte P, Itina T and Sentis M 2007 Laser-induced damage threshold of sapphire in nanosecond, picosecond and femtosecond regimes *Appl. Surf. Sci.* **254** 799–803

[44] Juodkazis S, Nishimura K, Misawa H, Ebisui T, Waki R, Matsuo S and Okada T 2006 Control over the crystalline state of sapphire *Adv. Mater.* **18** 1361–4

[45] Butkutė A, Sirutkaitis R, Gailevičius D, Paipulas D and Sirutkaitis V 2022 Sapphire selective laser etching dependence on radiation wavelength and etchant *Micromachines* **14** 7

[46] Deb B, Altay A, Gilliss S R, Munoz N E and Carter C B 2004 Technique for monitoring the etching rate of alumina *MRS Proc.* **819** N3.11

[47] Ćurković L, Jelača M F and Kurajica S 2008 Corrosion behavior of alumina ceramics in aqueous HCl and H_2SO_4 solutions *Corros. Sci.* **50** 872–8

[48] Liu X, Yang S, Yu L, Chen Q, Zhang Y and Sun H 2019 Rapid engraving of artificial compound eyes from curved sapphire substrate *Adv. Funct. Mater.* **29** 1900037

[49] Hörstmann-Jungemann M 2010 3D-microstructuring of sapphire using fs-laser irradiation and selective etching *J. Laser MicroNanoeng.* **5** 145–9

[50] Wortmann D, Gottmann J, Brandt N and Horn-Solle H 2008 Micro- and nanostructures inside sapphire by fs-laser irradiation and selective etching *Opt. Express* **16** 1517

[51] Liu X-Q, Zhang Y-L, Li Q-K, Zheng J-X, Lu Y-M, Juodkazis S, Chen Q-D and Sun H-B 2022 Biomimetic sapphire windows enabled by inside-out femtosecond laser deep-scribing *PhotoniX* **3** 1

[52] Juodkazis S, Nishi Y and Misawa H 2008 Femtosecond laser-assisted formation of channels in sapphire using KOH solution *Phys. Status Solidi* **2** 275–7

[53] Capuano L, Berenschot J W, Tiggelaar R M, Feinaeugle M, Tas N R, Gardeniers J G E and Römer G R B E 2022 Fabrication of microstructures in the bulk and on the surface of sapphire by anisotropic selective wet etching of laser-affected volumes *J. Micromech. Microeng.* **32** 125003

[54] Capuano L, Pohl R, Tiggelaar R M, Berenschot J W, Gardeniers J G E and Römer G R B E 2018 Morphology of single picosecond pulse subsurface laser-induced modifications of sapphire and subsequent selective etching *Opt. Express* **26** 29283

[55] Thapa J, Liu B, Woodruff S D, Chorpening B T and Buric M P 2017 Raman scattering in single-crystal sapphire at elevated temperatures *Appl. Opt.* **56** 8598

[56] Porto S P S and Krishnan R S 1967 Raman effect of corundum *J. Chem. Phys.* **47** 1009–12

[57] Schütt F *et al* 2020 Conversionless efficient and broadband laser light diffusers for high brightness illumination applications *Nat. Commun.* **11** 1437

[58] Alqurashi T, Sabouri A, Yetisen A K and Butt H 2017 Nanosecond pulsed laser texturing of optical diffusers *AIP Adv.* **7** 025313

[59] Zhou L, Liu S and Zhong T 2023 A comprehensive review of optical diffusers: progress and prospects *Nanoscale* **15** 1484–92

[60] Yamashita K, Taniguchi K, Hattori T, Kuwahara Y and Saito A 2023 Development of a high-performance, anti-fouling optical diffuser inspired by *Morpho* butterfly's nanostructure *Adv. Opt. Mater.* **11** 2301086

[61] Elsherif M, Hassan M U, Yetisen A K and Butt H 2018 Glucose sensing with phenylboronic acid functionalized hydrogel-based optical diffusers *ACS Nano* **12** 2283–91

[62] Elsherif M, Moreddu R, Hassan M U, Yetisen A K and Butt H 2019 Real-time optical fiber sensors based on light diffusing microlens arrays *Lab Chip* **19** 2060–70

[63] Ullah I, Lv H, Whang A J-W and Su Y 2017 Analysis of a novel design of uniformly illumination for Fresnel lens-based optical fiber daylighting system *Energy Build.* **154** 19–29

[64] Wachenfelt H V, Vakouli V, Diéguez' A P, Gentile N, Dubois M-C and Jeppsson K-H 2015 Lighting energy saving with light pipe in farm animal production *J. Daylight.* **2** 21–31

[65] Ai M, Youn J, Salcudean S E, Rohling R, Abolmaesumi P and Tang S 2019 Photoacoustic tomography for imaging the prostate: a transurethral illumination probe design and application *Biomed. Opt. Express* **10** 2588

[66] Nguyen T H, Rhee Y, Ahn J and Kang H W 2015 Circumferential irradiation for interstitial coagulation of urethral stricture *Opt. Express* **23** 20829